AIAA 79-1554R

Calculation of Unsteady Transonic Flow over an Airfoil

W. J. Chyu,* S. S. Davis,† and K. S. Chang‡
NASA Ames Research Center, Moffett Field, Calif.

An implicit finite-difference solver for either the Euler equations or the "thin-layer" Navier-Stokes equations was used to calculate a transonic flow over the NACA 64A010 airfoil pitching about its one-quarter chord. An unsteady automatic grid-generation procedure that will improve significantly the computational efficiency of various unsteady flow problems is described. The calculated results for both inviscid and viscous flows at Mach number 0.8 over the airfoil oscillating with reduced frequency referenced to one-half chord, 0.2, are compared with experimental data measured in the Ames 11×11-ft Transonic Wind Tunnel. Nonlinear, unsteady effects of the flow on the surface pressure variations, shock-wave excursions, and overall airloads are examined. Good agreements between the results of computations and experiments were obtained. In the shock-wave region, however, the results of the viscous-flow computations showed closer agreement with the experimental data.

Introduction

THE need to properly compute unsteady transonic viscous flows surrounding airfoils at transonic speeds remains an outstanding problem in fluid dynamics. Efficient and complete analytical methods would find immediate applications for both fixed-wing aircraft, in the treatment of such problems as flutter and buffet, and for rotary-wing aircraft in optimizing rotor-blade designs.

Mathematically, even within an inviscid approximation, the analysis of steady transonic flows is complicated by the presence of mixed subsonic and supersonic regions within the flowfield. Consideration of unsteady transonic flows necessitates treatment of additional phenomena such as moving shock waves whose strengths are time varying. In addition, for those flows such as flutter, buffet, and dynamic stall where viscous effects are significant, the unsteady inviscid-viscous interaction must be modeled properly.

Numerous researchers have studied unsteady transonic flows around airfoils (cf. Ref. 1 for a recent bibliography) using a variety of numerical techniques based on the inviscid and viscous equations which model the physics at various levels of approximation. The inviscid techniques include methods based, successively, on the linear small-disturbance equations,[2,3] and on the low-frequency small-disturbance equations,[4-6] which are limited to the cases of having weak shock waves in inviscid flows. Additional modeling accuracy is obtained with methods based on the unsteady full-potential equations[7,8] which remove the restriction of weak shock waves. The next level of modeling accuracy is demonstrated by Magnus and Yoshihara[9] and Lerat and Sides[10] in their solutions of unsteady transonic flow over an airfoil based on the Euler equations. Although their solutions represent a pioneering work in showing the unsteady nonlinear response of the flows, the computation time is excessively long with regard to the inclusion of viscous effects or extension to three-dimensional flows. Both methods based on the potential equations and on the Euler equations, in principle, can treat all unsteady transonic flows in which viscous effects are not significant. For those cases where viscous effects dominate, methods based on the unsteady Navier-Stokes equations are needed. Mehta[11] used a method based on the incompressible Navier-Stokes equations to compute the laminar flow about an airfoil undergoing large amplitude oscillations. The results provide an extremely valuable insight into the phenomena of dynamic stall on helicopter rotors. Beam and Warming[12] reported an efficient numerical solution of the compressible Navier-Stokes equations in conservative-law form. They developed an implicit-factorization scheme that allows large time steps to be taken in the unsteady flow computations while maintaining second-order accuracy. Their computation considered the flow about a parabolic airfoil and an oscillating flat plate, both computed in the physical plane. Steger[13] applied an implicit numerical technique, similar to the one reported in Ref. 12, to both the unsteady Euler equations and the unsteady thin-layer viscous model compressible Navier-Stokes equations. The inviscid-flow computation considered the plunging airfoil previously reported in Ref. 9, while the viscous-flow computation demonstrated unsteady transonic buffet behind a fixed airfoil.

The purpose of this study was to develop a numerical technique for analyzing unsteady transonic flows over an arbitrary airfoil when both unsteady and viscous effects are significant. Toward this end, the numerical technique reported by Steger[13] was combined with an efficient unsteady grid-generation technique suitable for the treatment of moving and deforming airfoils. The resulting method was applied to compute both inviscid and viscous transonic flows about an NACA 64A010 airfoil oscillating in pitch. The computations were carried out for flow conditions where extensive experimental unsteady surface pressure distributions had been obtained.[14,15] The numerical technique and a comparison of the numerical results with the experimental measurements are discussed in the following sections.

Numerical Technique

Governing Equations

The unsteady flowfield is assumed to obey the unsteady Navier-Stokes equations. Following Ref. 13, these equations can be written in strong conservation-law form for body-conforming coordinates ξ, η as

$$\partial_\tau \hat{q} + \partial_\xi \hat{E} + \partial_\eta \hat{F} = Re^{-1} \partial_\eta \hat{S} \tag{1}$$

where $\tau = t$ is the time variable, $\xi = \xi(x,y,t)$ the "streamwise" spatial coordinate (see Fig. 1), and $\eta = \eta(x,y,t)$ the "normal" spatial coordinate. The inviscid flux vectors in Eq. (1) are

Presented as Paper 79-1554 at the AIAA 12th Fluid and Plasma Dynamics Conference, Williamsburg, Va., July 23-25, 1979; submitted Dec. 13, 1979; revision received Dec. 10, 1980. This paper is declared a work of the U.S. Government and therefore is in the public domain.

*Research Scientist, Aerodynamic Research Branch. Member AIAA.

†Research Scientist, Aerodynamic Research Branch. Associate Fellow AIAA.

‡National Research Council Research Associate.

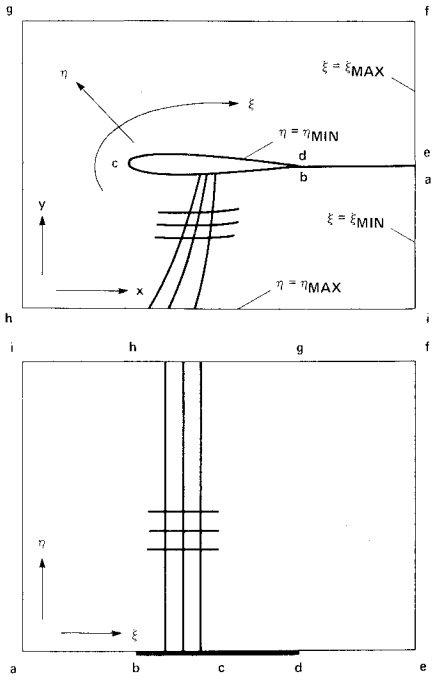

Fig. 1 Physical and computational planes.

$$\hat{q}=J^{-1}\begin{pmatrix}\rho\\ \rho u\\ \rho v\\ e\end{pmatrix},\quad \hat{E}=J^{-1}\begin{pmatrix}\rho U\\ \rho uU+\xi_x p\\ \rho vU+\xi_y p\\ (e+p)U-\xi_t p\end{pmatrix}$$

$$\hat{F}=J^{-1}\begin{pmatrix}\rho V\\ \rho uV+\eta_x p\\ \rho vV+\eta_y p\\ (e+p)v-\eta_t p\end{pmatrix} \tag{2}$$

with the contravariant velocity components defined in terms of the Cartesian velocities as

$$U=\xi_t+\xi_x u+\xi_y v \quad V=\eta_t+\eta_x u+\eta_y v \tag{3}$$

The mapping between x,y physical plane and the ξ,η computational plane is reflected in Eq. (1) through the presence of the metric terms ξ_t, ξ_x, ξ_y, η_t, η_x, η_y, and the Jacobian term J which appear in the flux vectors. The metric and Jacobian terms are determined numerically once the instantaneous x,y coordinates of the grid points within the computational mesh have been specified. The method of generating the time-varying computational mesh is discussed subsequently.

In deriving Eq. (1), Steger assumed a thin-layer viscous model by neglecting all streamwise derivatives $\partial(\ )/\partial\xi$ in the viscous terms of the Navier-Stokes equations. The resulting thin-layer viscous model, valid for high Reynolds number flow and body-conforming coordinate, is

$$\hat{S}=J^{-1}\begin{Bmatrix}0\\ \mu(\eta_x^2+\eta_y^2)u_\eta+(\mu/3)(\eta_x u_\eta+\eta_y v_\eta)\eta_x\\ \mu(\eta_x^2+\eta_y^2)v_\eta+(\mu/3)(\eta_x u_\eta+\eta_y v_\eta)\eta_y\\ \{(\eta_x^2+\eta_y^2)[(\mu/2)(u^2+v^2)_\eta+\kappa P_r^{-1}(\gamma-1)^{-1}\\ \times(a^2)_\eta]+(\mu/3)(\eta_x u+\eta_y v)(\eta_x u_\eta+\eta_y v_\eta)\}\end{Bmatrix} \tag{4}$$

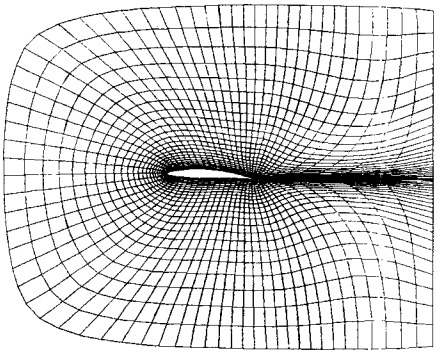

Fig. 2 Grids generated using uniform coordinate stretching method.

For laminar flow computations, the coefficients of molecular viscosity appearing in Eq. (4) is computed using the Sutherland viscosity law. For turbulent flows, the viscosity coefficient is computed using the two-layer Cebeci-type eddy viscosity model reported by Baldwin and Lomax.[16] The main features of the Baldwin-Lomax model are the determination of the eddy mixing-length scale based on the local vorticity and automatic determination of the edge of the boundary layer. In the present work, the instantaneous vorticity is calculated after each time step of the computation.

Equation (1) is integrated in time, subject to appropriate initial conditions and boundary conditions using an approximately factored implicit finite-difference algorithm, similar to the one reported by Beam and Warming.[12] A complete description of the algorithm, including a discussion of its accuracy and stability, is found in Ref. 13.

Boundary Conditions

For inviscid flow computations, Eq. (4) is neglected in Eq. (1) and a tangency condition is imposed on the airfoil surface by setting V, the contravariant velocity along the η coordinate, to zero. Thus, on the surface, the Cartesian velocities are

$$\begin{pmatrix}u\\ v\end{pmatrix}=J^{-1}\begin{bmatrix}\eta_y & -\xi_y\\ -\eta_x & \xi_x\end{bmatrix}\begin{pmatrix}U-\xi_t\\ -\eta_t\end{pmatrix} \tag{5}$$

In Eq. (5), U is determined at the body surface by a linear extrapolation from the flowfield determined at the previous time step, and

$$\xi_t=-x_\tau\xi_x-y_\tau\xi_y \quad \eta_t=-x_\tau\eta_x-y_\tau\eta_y \tag{6}$$

where x_τ and y_τ are local airfoil surface velocities. At the trailing edge of the airfoil, the Cartesian velocities u,v are set equal to x_τ and y_τ, respectively, to satisfy the Kutta condition.

For viscous flow, the no-slip condition requires $U=V=0$ at the airfoil surface. The surface pressure is then determined from the normal momentum equation.

Grid Generation

In the work reported in Ref. 13, the computational grids were obtained from solutions of a nonlinear Poisson equation. This technique[17,18] permits grid point locations to be specified along the outer edge of the grid, i.e., along the airfoil surface and the freestream boundary (cf. Fig. 1). The method then generates a smoothly spaced, nonoverlapping grid at the interior points. This grid is then respaced, or clustered, along the $\xi=$const lines (lines moving away from the airfoil) to obtain a grid having a fine spacing at the airfoil suitable for viscous-flow computation. The resulting grid is stored and used for the flowfield computation. Proper clustering of grid points in the vicinity of the airfoil is essential for obtaining accurate viscous solutions. In Ref. 13, clustering was achieved with an exponential stretching of

points along $\xi = \text{const}$ lines based on coordinate arc lengths between the airfoil and the chosen outer boundary of the grid. The same exponential stretching formula was applied at all chordwise stations. In some instances this procedure results in grids which are excessively dense toward the trailing edge of the airfoil and in the wake region. Figure 2 shows a body-conforming grid generated using the method described in Ref. 13. The grid point spacing is needlessly dense in the far wake region. Also, the $\eta = \text{const}$ lines are warped behind the airfoil, and this effect is propagated to the outer boundary. To achieve better control of the grid spacing, a weighted coordinate stretching is employed in the present work. The exponential stretching along $\xi = \text{const}$ lines was a weighted average between a stretching based on coordinate arc length and a stretching based on the vertical distance y between the airfoil surface and the outer boundary. Further, the exponential stretchings employed varied smoothly with chordwise position. The stretching is made along each $\xi = \text{const}$ line using a weighted exponential stretching function $T(\eta)|_\xi$ defined as

$$T_1 = 0$$

$$T_k = T_{k-1} + \Delta T_{\min}(1+\epsilon)^{k-2} \quad 2 \le k \le k_{\max} \tag{7}$$

where

$$T_k(x_k, y_k) = \gamma(y_{\max})A_k + \delta(y_{\max})|y_k| \tag{8}$$

Here, k is the index of the kth line of constant η (cf. Fig. 1), A_k the arc length measured from the airfoil surface along the $\xi = \text{const}$ line, and $y_{\max}$ the maximum y coordinate on the $\xi = \text{const}$ line. The parameters γ and δ weight the stretching between arc length and vertical distance y, respectively. A smooth variation of the parameters with chordwise position is obtained using

$$\gamma(y_{\max}) = \tfrac{1}{2}[1 + \cos(|y_{\max}|\pi/|y_{cr}|)]$$

$$\delta(y_{\max}) = 1 - \gamma(y_{\max}) \tag{9}$$

for $|y_{\max}| \le |y_{cr}|$, and $\gamma = 0$ and $\delta = 1$ for $|y_{\max}| > |y_{cr}|$ where y_{cr} is a parameter for controlling the grid spacing.

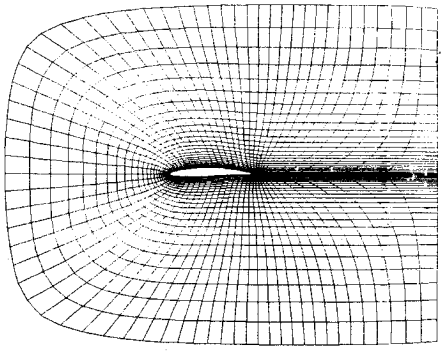

Fig. 3 Grids generated using weighted coordinate stretching method.

The weighted minimum spacing at the airfoil surface $\Delta T_{\min}$ is defined by

$$\Delta T_{\min} = \gamma(y_{\max})\Delta A + \delta(y_{\max})|\Delta y| \tag{10}$$

in terms of ΔA, the minimum spacing along the $\xi = \text{const}$ line, and Δy, the minimum spacing in the y direction. The stretching parameter ϵ is determined such that

$$T_{k_{\max}} = \gamma(y_{\max})A_{k_{\max}} + \delta(y_{\max})|y_{k_{\max}}| \tag{11}$$

using a Newton-Raphson iterative procedure.

A coordinate system generated using the weighted coordinate stretching technique applied to airfoil and outer boundary grid points identical to those of Fig. 2 is shown in Fig. 3, and demonstrates improved grid spacing and clustering.

In Ref. 13, the grid geometry was held constant in time. Time variation of the angle of attack of an oscillating airfoil was accomplished by varying the far-field freestream boundary conditions. Although this approach to grid generation would be suitable for the present study, it is limited in scope insofar as it cannot treat an airfoil oscillating in the proximity of a wall or a second airfoil, or a flap oscillating behind a fixed airfoil. Thus, in the present work, an alternative, more general approach was adopted. The outer boundaries of the grid were held fixed in space and time, while the airfoil position varied in time. The grid, in turn, deformed as time progressed to follow the motion of the airfoil.

Allowing the airfoil surface to vary within a stationary outer boundary requires that a new grid be generated at each time step of the computation. To reduce the computational effort needed to repeatedly generate the grids, a novel grid interpolation scheme was devised. Grids were generated at the extreme angle-of-attack positions of the prescribed airfoil motion using the Poisson equation and weighted coordinate stretching techniques described previously, and stored. Grids needed at intermediate airfoil angles of attack were found from interpolation along the circular arcs that are assumed to represent the locus of grid point movement. The radius of curvature for each point of the grid was taken as the distance between the grid point and the fixed pivot point about which the airfoil was oscillating. With the radius of curvature and the extreme positions of each grid point known, the center of curvature was then computed for each grid point. Grid points for intermediate values of the angle of attack were found from a linear interpolation of arc length along the curves defined in this manner. This method of grid interpolation eliminated entanglement of coordinate lines during the airfoil motion, even within the dense grids in the boundary-layer region. An example of the interpolation method is shown in Fig. 4. Grids similar to those used in computations obtained at the extreme positive and negative angle-of-attack positions are shown in Figs. 4a and b, respectively, while an interpolated grid is shown in Fig. 4c.

Results

Experimental Measurements

A series of experimental measurements has been carried out in the Ames 11×11-ft transonic wind tunnel. In these ex-

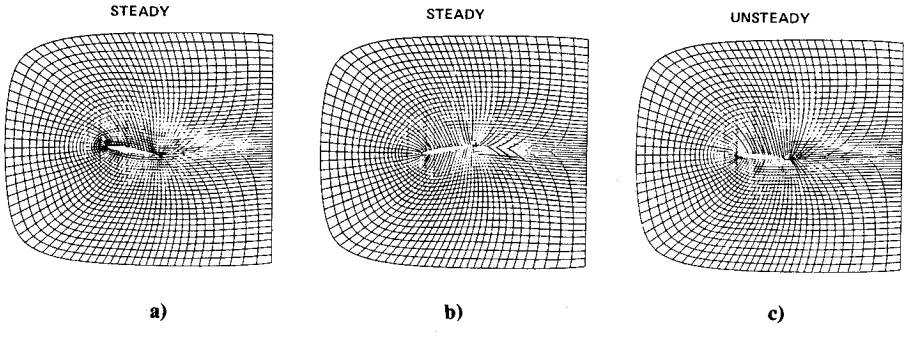

Fig. 4 Unsteady grids interpolated from two steady-grid systems: a) steady grids with airfoil at one extreme position, b) steady grids with airfoil at another extreme position, and c) unsteady grids interpolated from a and b.

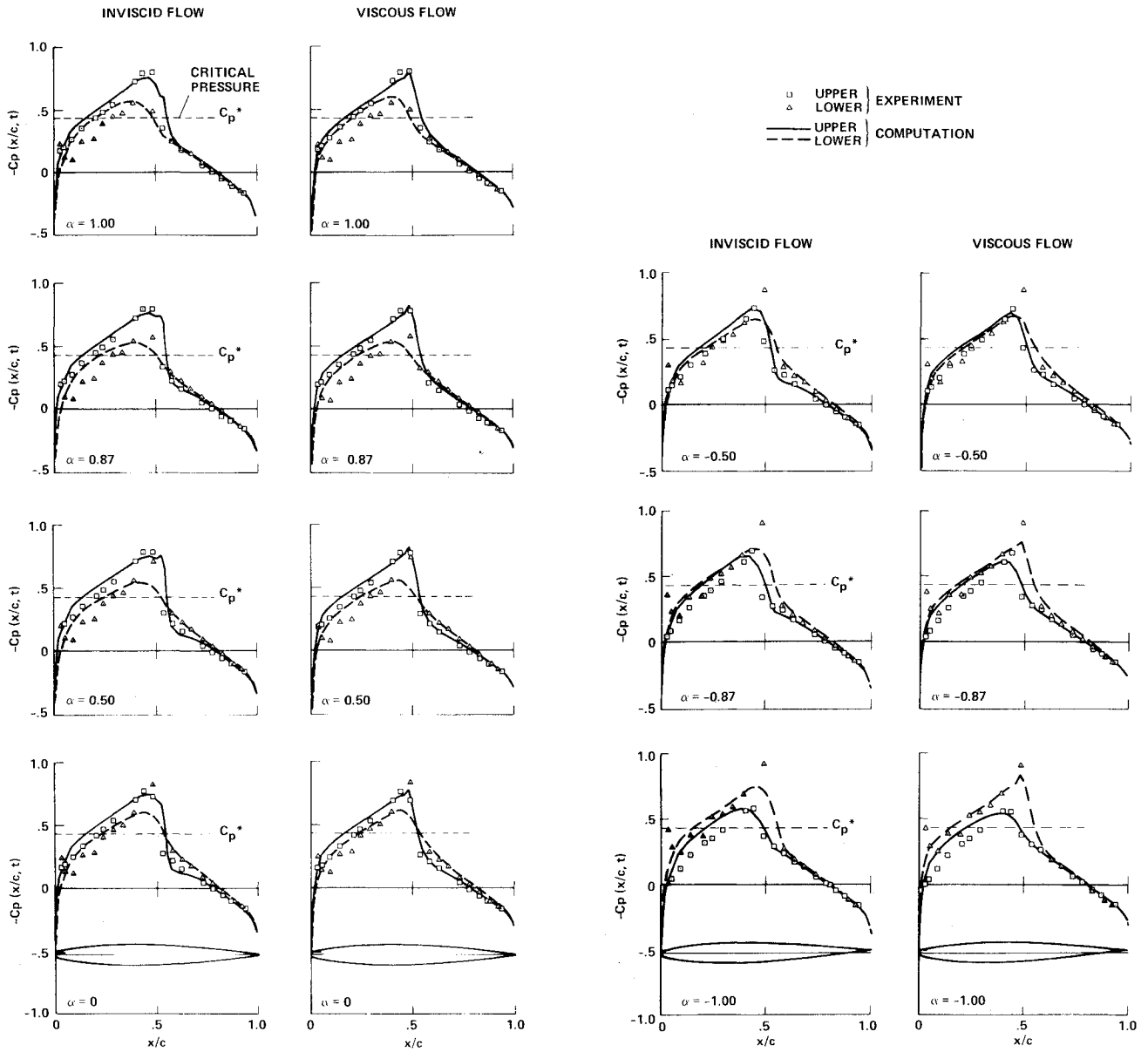

Fig. 5 Time histories of surface pressures.

periments, an NACA 64A010 airfoil was caused to undergo small-amplitude harmonic oscillations in pitch about fixed pivot points located at $x/c = 0.25$, and also to undergo oscillations in plunge. The test Mach numbers ranged from 0.5 to 0.8, and Reynolds numbers based on the airfoil chord ranging from 2.5×10^6 to 12.5×10^6 were obtained. Unsteady pressure distributions were measured on the airfoil during the course of the oscillations, and unsteady aerodynamic forces and moments were obtained subsequently from spatial integration of the pressure distributions.

The case of interest for the present study was chosen as the airfoil oscillating in pitch about a pivot point fixed at $x/c = 0.25$, with amplitude of oscillation of 1 deg and a mean value of the pitch angle of zero. (With the pivot point fixed, the pitch angle is equivalent to the airfoil's angle of attack.) The reduced frequency of the oscillation, $\omega c/2U_\infty$, was taken as 0.20, while the Mach and Reynolds numbers were held fixed at $M = 0.8$ and $Re = 12.0 \times 10^6$.

Computations and Code Performance

Both inviscid and viscous unsteady computations were carried out for the flow conditions previously outlined. The computational grids have common outer boundary located 8 chord lengths above and below the airfoil, and 8 chord lengths upstream and downstream from the airfoil leading edge. The inviscid computation used a grid having 77 points in the ξ direction and 26 points in the η direction. The computation required 1.27 s on a CDC 7600 per iteration, and 600 iterations were required to model one cycle of oscillation, for a total computation time of 12.7 min per cycle. The unsteady computations were started from a converged steady-flow solution obtained at $\alpha = 1$ deg and required computing through two cycles of oscillation to reach the periodic solution.

The viscous computations were made using a grid having 87×41 points in the ξ and η directions, respectively. Including the viscous terms requires additional computational effort per grid point, and the fine mesh, needed to resolve the boundary-layer region, necessitated a smaller time step than the one used in the inviscid computations. Thus, the viscous computations required 4.33 s per iteration, 1800 iterations per cycle, and 130 min per cycle. Again, computations through two cycles of oscillation were required to obtain the periodic solution.

Time Histories of Surface Pressure and Shock-Wave Excursion

Computed viscous and inviscid surface pressure distributions, obtained as the airfoil angle of attack varied from 1 to -1 deg, are shown in Fig. 5. Also shown in Fig. 5

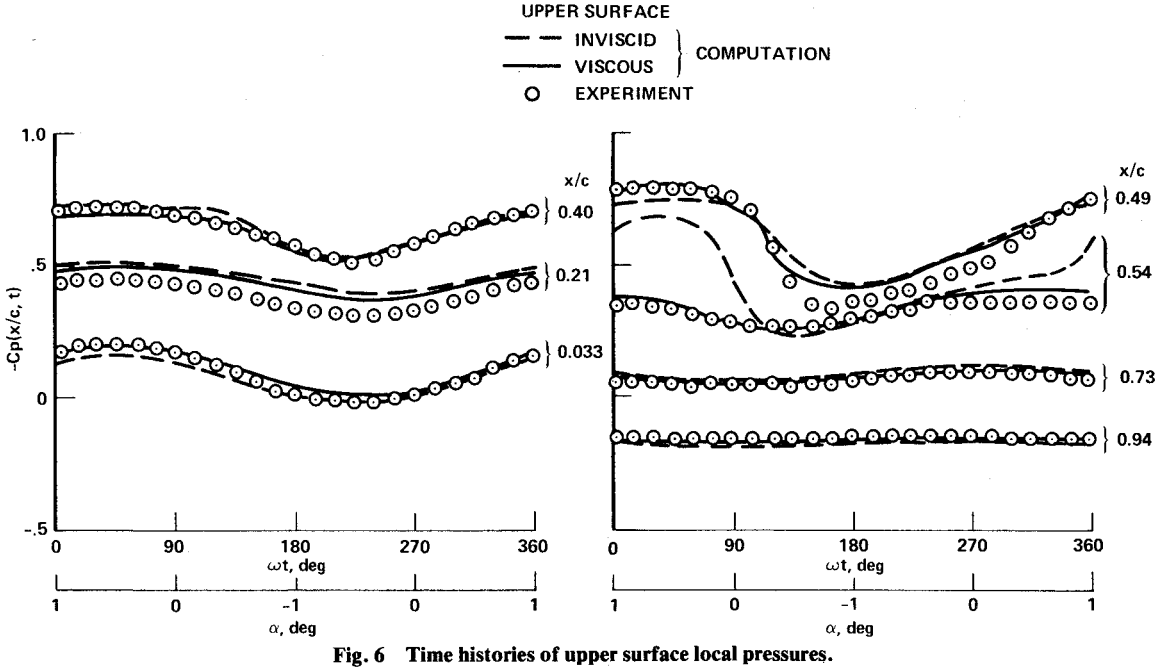

Fig. 6 Time histories of upper surface local pressures.

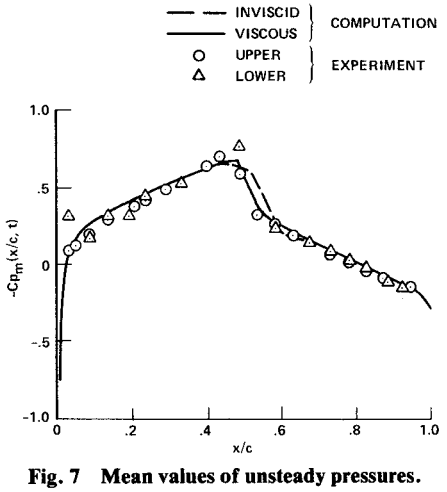

Fig. 7 Mean values of unsteady pressures.

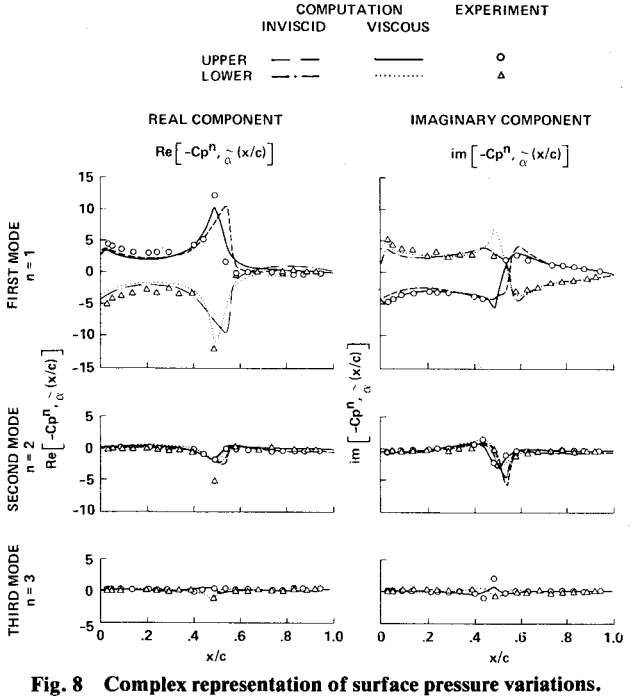

Fig. 8 Complex representation of surface pressure variations.

are experimentally measured pressure distributions. Results are presented for only one-half cycle of oscillation in Fig. 5, because in this symmetrical case the lower surface pressure distributions in the next half cycle are 180 deg out of phase and thus can be obtained from the upper surface pressure distributions shown. At the maximum value of the airfoil angle of attack, $\alpha = 1$ deg, a supersonic region is evident on the upper surface that terminates in a shock located at $x/c = 0.55$. As the angle of attack decreases, the flow speed gradually decreases on the upper surface, with corresponding increases in pressure. At the same time, the shock strength decreases, as evidenced by the decrease of the pressure rise at the shock. In contrast, the flow speed on the lower surface of the airfoil increases, resulting in lower surface pressures, and the flow pattern is reversed. The comparisons between the computational results and the experimental measurements show that the computed pressures ahead of the upper surface shock are underpredicted, although the viscous flow results agree more closely with the experimental results. In the shock-wave region the pressure rises, and shock positions are well predicted by the viscous computations. The pressure distributions downstream of the shock are well predicted by both computations for this case in which there is no flow separation. Although the effects of the shock-wave boundary-layer interaction must be taken into account to accurately model the pressure distribution in the vicinity of the shock, they are less important in the other regions of the flow.

The time variation of the computed and experimentally measured surface pressure distributions can be expressed in terms of Fourier components in-phase and 90 deg out-of-phase with the unsteady angle of attack. The unsteady angle of attack can be expressed as

$$\alpha(t) = \alpha_m + \mathrm{Re}(\tilde{\alpha} e^{i\omega t}) \tag{12}$$

where α_m is the mean value of the angle of attack and $\tilde{\alpha}$ is the (real) unsteady component. The Fourier series representation of the surface pressure coefficient is

$$C_p(x/c,t) = C_{p_m}(x/c) + \sum_{n=1}^{\infty} \mathrm{Re}\{[C^n_{p,\tilde{\alpha}}(x/c)]\,\tilde{\alpha} e^{in\omega t}\} \tag{13}$$

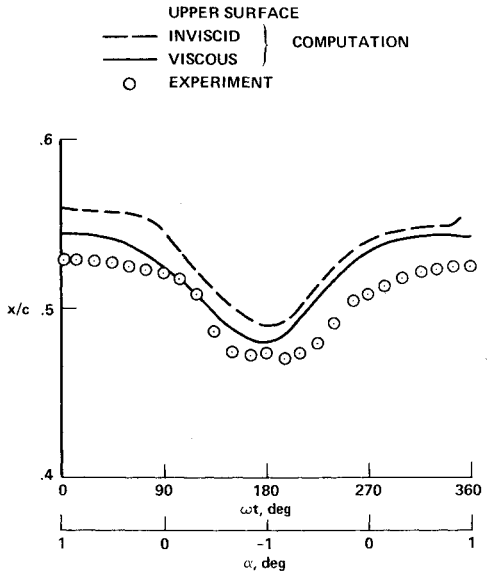

Fig. 9 Shock locus on upper surface of the airfoil.

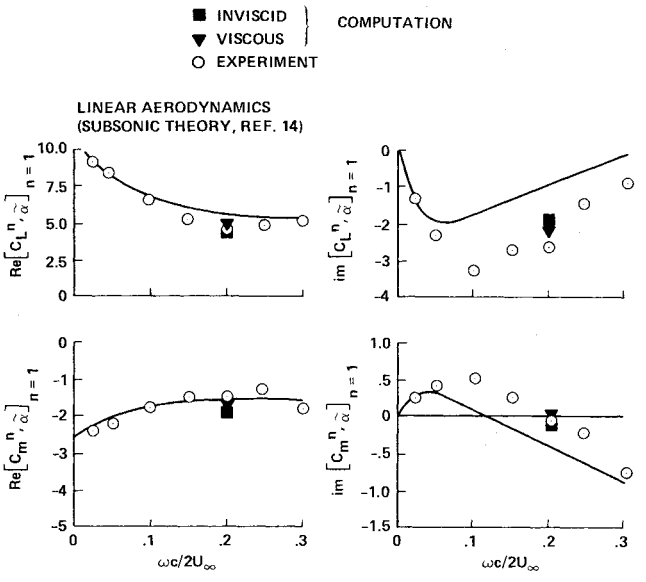

Fig. 10 Aerodynamic transfer function.

where $C_{pm}(x/c)$ is the mean value of the local surface pressure coefficient and $[C^n_{p,\tilde{\alpha}}(x/c)]$ the nth complex component of the local unsteady pressure coefficient, per radian. The real and imaginary value of $C^n_{p,\tilde{\alpha}}$ can be expressed as

$$\mathrm{Re}[C^n_{p,\tilde{\alpha}}(x/c)] = (C^n_p/\tilde{\alpha})\cos\phi_n \tag{14a}$$

and

$$\mathrm{Im}[C^n_{p,\tilde{\alpha}}(x/c)] = (C^n_p/\tilde{\alpha})\sin\phi_n \tag{14b}$$

where C^n_p is the nth harmonic unsteady pressure (real) and ϕ_n is the nth harmonic phase shift between the angle of attack and the pressure response.

Computed and experimentally measured time histories of the local pressure coefficient on the upper surface of the airfoil for a complete cycle of oscillation are shown in Fig. 6. The pressure coefficients on the surface ahead of and behind the shock wave display a sinusoidal variation which can be satisfactorily represented by the first harmonic ($n=1$) of the Fourier series. In the shock region, on the other hand, the pressure variations are nonlinear, and three Fourier harmonics are usually required to represent the time histories. The pressure variations behind the shock wave are small compared with those occurring in front of the shock, and decrease gradually with distance toward the trailing edge of the airfoil.

Both the computed and unmeasured unsteady pressures have been expressed in Fourier components up to and including the third harmonic. The mean pressures shown in Fig. 7 are reasonably well predicted except in the shock region where the viscous flow computation shows a closer agreement with the experimental data. The harmonic components of the pressure are plotted as the real and imaginary parts in Fig. 8. The modal content decreases rapidly with the increasing order of the mode number. In practice, only the first two modal components would be required to represent the surface pressure except in the region of the shock wave where all three components would be required. The best agreement with the experimental data is provided by using the Navier-Stokes equations.

Examination of the in-phase and 90 deg out-of-phase components in the first mode $\mathrm{Re}[C^n_{p,\tilde{\alpha}}(x/c)]_{n=1}$ and $\mathrm{Im}[C^n_{p,\tilde{\alpha}}(x/c)]_{n=1}$, respectively, in Fig. 8 indicates that the pressures in front of the shock wave contain both the in-phase and out-of-phase components in about equal magnitude. Pressures behind the shock wave, however, contain only the out-of-phase components. The first mode out-of-phase components in Fig. 8 also show that the component in front of the shock is 180 deg out-of-phase with those behind the shock and that the phase shift abruptly takes place at the shock.

The loci of the computed and measured shock-wave excursions are shown in Fig. 9. The trend of the excursions is well predicted by either the inviscid- or viscous-flow computations. The results of the viscous computation, however, agree more closely with the experimental data.

The aerodynamic transfer function for lift and pitching-moment coefficients $C_{L,\tilde{\alpha}}$ and $C_{m,\tilde{\alpha}}$ computed with the Euler and Navier-Stokes equations and expressed in terms of complex variables similar to those in Eqs. (14) are compared with the experimental data in Fig. 10. The viscous-flow computations result in excellent agreement with the experimental data. The less agreement of inviscid-flow computations (including the results from linear theory) with the experimental data is caused by the inability to accurately predict the shock strength and locations.

Concluding Remarks

An implicit finite-difference solver for either the Euler equations or the "thin-layer" Navier-Stokes equations was used to calculate a transonic flow over the NACA 64A010 airfoil pitching about its one-quarter chord. An unsteady automatic grid-generation procedure was developed and combined with the solver to greatly improve the efficiency of unsteady flow computations. A weighted coordinate-stretching technique was used to generate well regulated and controlled grids over the entire flowfield including the clustered region near the boundary layer. The computational results for both inviscid and viscous flows at $M_\infty = 0.8$ over the airfoil oscillating with reduced frequency, $\omega c/2U_\infty = 0.2$, are compared with experimental data from the Ames 11×11-ft transonic wind tunnel. Nonlinear unsteady characteristics of the surface pressures, shock-wave excursions, and overall airloads are examined. The study shows that the computational results, both the inviscid and viscous flows, are in good agreement with the experimental data except in the shock-wave region. There the effects of shock boundary-layer interaction must be taken into account to accurately model the pressure distribution and shock position. The aerodynamic transfer function of overall airloads in terms of lift and pitching-moment coefficient are, therefore, more accurately predicted by the viscous-flow computation. Finally, the efficiency of the numerical algorithm is demonstrated by the relatively short computing time required for both the inviscid and viscous-flow computations.

Acknowledgments

The authors are grateful to Leroy L. Presley, Michael Tauber, and Lewis B. Schiff for their valuable comments and suggestions.

References

[1] Borland, C. J., "A Bibliography of Recent Developments in Unsteady Transonic Flow," AFFDL-TR-78-189, Vol. 1, Feb. 1979.

[2] Ehlers, F. E., "A Finite Difference Method for the Solution of the Transonic Flows Around Harmonically Oscillating Wings," NASA CR-2257, Jan. 1974.

[3] Traci, R. M., Farr, J. L., and Albano, E., "Perturbation Method for Transonic Flows About Oscillating Airfoils," AIAA Paper 75-877, June 1975.

[4] Ballhaus, W. F. and Goorjian, P. M., "Implicit Finite Difference Computations of Unsteady Transonic Flows about Airfoils Including the Treatment of Irregular Shock Wave Motions," AIAA Paper 77-205, Jan. 1977.

[5] Rizzetta, D. P. and Chin, W. C., "Effect of Frequency in Unsteady Transonic Flow," *AIAA Journal*, Vol. 17, July 1979, pp. 779-781.

[6] Rizzetta, D. P. and Yoshihara, H., "Computation of the Pitching Oscillation of an NACA 64A010 Airfoil in the Small Disturbance Limit," AIAA Paper 80-0128, Jan. 1980.

[7] Isogai, K., "Calculation of Unsteady Transonic Flow Using the Full Potential Equation," AIAA Paper 77-448, March 1977.

[8] Goorjian, P. M., "Implicit Computation of Unsteady Transonic Flow Governed by the Full Potential Equation in Conservative Form," AIAA Paper 80-150, Jan. 1980.

[9] Magnus, R. and Yoshihara, H., "Unsteady Flows over an Airfoil," *AIAA Journal*, Vol. 13, Dec. 1975, pp. 1622-1628.

[10] Lerat, A. and Sides, J., "Numerical Calculation of Unsteady Transonic Flows," AGARD Meeting of Unsteady Airloads in Separated and Transonic Flow, Lisbon, Portugal, April 17-22, 1977.

[11] Mehta, U. B., "Dynamic Stall of an Oscillating Airfoil," AGARD Fluid Dynamics Panel Symposium on Unsteady Aerodynamics, Ottawa, Can., Sept. 1977.

[12] Beam, R. and Warming, R. F., "An Implicit Finite Difference Algorithm for Hyperbolic Systems in Conservation Law Form," *Journal of Computational Physics*, Vol. 22, Sept. 1976, pp. 87-110.

[13] Steger, J., "Implicit Finite-Difference Simulation of Flow About Arbitrary Two-Dimensional Geometrics," *AIAA Journal*, Vol. 16, July 1978, pp. 679-686.

[14] Davis, S. S. and Malcolm, G. N., "Transonic Shock-Wave/Boundary Layer Interactions on an Oscillating Airfoil," *AIAA Journal*, Vol. 18, Nov. 1980, pp. 1306-1312.

[15] Davis, S. S. and Malcolm, G. N., "Unsteady Aerodynamics of a Conventional and Supercritical Airfoil," AIAA Paper 80-734, May 1980.

[16] Baldwin, B. S. and Lomax, H., "Thin Layer Approximation and Algebraic Model for Separated Turbulent Flows," AIAA Paper 78-257, 1978.

[17] Thompson, J. F., Thames, F. C., and Mastin, C. W., "Automatic Numerical Generation of Body-Fitted Curvilinear Coordinate System for Field Containing any Number of Arbitrary Two-Dimensional Bodies," *Journal of Computational Physics*, Vol. 15, July 1974, pp. 299-319.

[18] Sorensen, R. L. and Steger, J. L., "Simplified Clustering of Nonorthogonal Grids Generated by Elliptic Partial Differential Equations," NASA TM-73252, Aug. 1977.